

Session 22 Overview: *Terahertz for Communication and Sensing*

WIRELESS SUBCOMMITTEE



Session Chair:
Q. Jane Gu
University of California, Davis, CA



Session Co-Chair:
Byung-Wook Min
Yonsei University, Seoul, Korea



Session Moderator:
Maryam Tabesh
Google, Mountain View, CA

With the continuing advancements of THz technologies in silicon processes, this year's papers further push the technique frontiers in circuit performances and system demonstrations. This session features four THz papers describing THz Prism for spectrum-to-space mapping, 300GHz wideband communication, a 0.42THz coherent transceiver for phase-contrast imaging, and a phase-processing-based micrometer-range-resolution radar at 250GHz.

8:30 AM

22.1 THz Prism: One-Shot Simultaneous Multi-Node Angular Localization Using Spectrum-to-Space Mapping with 360-to-400GHz Broadband Transceiver and Dual-Port Integrated Leaky-Wave Antennas

Hooman Saeidi, Princeton University, Princeton, NJ

In Paper 22.1, Princeton University demonstrates THz Prism: one-shot simultaneous multi-node angular localization using spectrum-to-space mapping and dual-port integrated leaky-wave antennas in 65nm CMOS. A one-shot direction-finding across 1D with an accuracy of 0.95deg and 2.1deg with an integration time of 5ms and 50 μ s respectively is demonstrated.



8:38 AM

22.2 A 300GHz-Band Phased-Array Transceiver Using Bi-Directional Outphasing and Hartley Architecture in 65nm CMOS

Ibrahim Abdo, Tokyo Institute of Technology, Tokyo, Japan

In Paper 22.2, Tokyo Institute of Technology and NTT present a 300GHz phased-array transceiver using outphasing and Hartley architecture in 65nm CMOS. This work demonstrates the first implementation of a wideband CMOS phased-array transceiver that operates at a frequency higher than 200GHz.



8:46 AM

22.3 A 0.42THz Coherent TX-RX System Achieving 10dBm EIRP and 27dB NF in 40nm CMOS for Phase-Contrast Imaging

Dragan Simic, KU Leuven - MICAS, Leuven, Belgium

In Paper 22.3, KU Leuven presents a 0.42THz coherent TX-RX system for phase-contrast imaging implemented in 40nm CMOS, achieving 52dB SNR (100kHz RBW) at 25cm distance thanks to the 10dBm EIRP TX and the 27dB NF RX.



22

8:54 AM

22.4 A 250GHz Autodyne FMCW Radar in 55nm BiCMOS with Micrometer Range Resolution

S. M. Hossein Naghavi, University of Michigan, Ann Arbor, MI

In Paper 22.4, the University of Michigan and STMicroelectronics report a 250GHz autodyne FMCW radar in 55nm BiCMOS with micrometer-range resolution using a phase processing method. With +17dBm maximum TX EIRP and 66.7GHz bandwidth, a range resolution of 54 μ m is achieved for targets at 25.4cm distance, with an overall measured range error better than 0.025%.



22.1 THz Prism: One-Shot Simultaneous Multi-Node Angular Localization Using Spectrum-to-Space Mapping with 360-to-400GHz Broadband Transceiver and Dual-Port Integrated Leaky-Wave Antennas

Hooman Saeidi*, Suresh Venkatesh*, Xuyang Lu, Kaushik Sengupta

Princeton University, Princeton, NJ

*Equally-Credited Authors (ECAs)

The spectrum above 100GHz is expected to spawn a generation of ultra-high-speed wireless links and intelligent sensing and imaging applications. They are meant to be supported through a heterogeneous and dynamically reconfigurable wireless network fabric in 5G and beyond. Such wireless communication and sensing applications require rapid localization and direction finding of mobile nodes [1]. This functionality is paramount for communications-on-the-move applications, wireless link discovery, and rapid beam alignment/tracking at mm-wave and THz frequencies [2-9]. The current protocols for direction finding and beam alignment in 5G mm-wave systems are based on iterative algorithms that are often non-scalable, time-consuming, and computationally expensive, posing serious challenges for low-latency applications. Thus there is a need to process such direction-finding methods at the 'edge nodes', to enable secure scalable networks with very low latencies [10]. In this article, we present a spectrum-to-space mapping principle, where localization information can be processed at the edge 'sensor node' through the spectrum sensing. The conceptual idea is presented in Fig. 22.1.1, which shows an access point (transmitter/receiver) that acts as a THz prism casting different spectral portions of a broadband THz signal across space. If the mapping is unique, multiple edge nodes can *simultaneously* localize themselves in a single-shot fashion through localized spectrum sensing, avoiding the use of the slow iterative process and bi-directional communication. In this paper, we present a scalable 360-to-400GHz transceiver architecture in 65nm CMOS with frequency-dependent beam synthesis using two dual-port integrated frequency-dispersive leaky-wave antennas. The two antennas when excited/sensed across the two opposite end-ports, cover a 1D spatial angle across $\pm 40^\circ$, and enable 2D localization with two such ICs covering both orthogonal basis vectors with a frequency-offset radiation (Fig. 22.1.1). Exploiting the cross-correlation of the spectrum-to-space mapping (Fig. 22.1.1), the system achieves 2D localization accuracy of $\sigma_\phi = 1.9^\circ$ and $\sigma_\Theta = 1.95^\circ$ for a measurement resolution bandwidth (RBW) of 20Hz.

The architecture of the chip is shown in Fig. 22.1.2. The chip consists of two leaky-wave antennas (LWA) whose two ends are fed by on-chip broadband signal synthesis and reception capability across 360 to 400GHz. The off-chip LO signal of 0dBm across 59 to 71GHz is converted into a differential on-chip signal, and amplified by 3-stage differential power amplifiers (PA). The PA has a simulated gain of 19.9dB, with P_{sat} of 15.52dBm and a peak PAE of 25.9%. The amplified differential signal is then fed to a doubler across 118 to 142GHz followed by an on-chip balun and a tripler stage. The combination of the doubler-tripler generates a measured peak power of -10.9dBm across 360 to 400GHz. The single-ended output of the tripler is then impedance matched and fed to the LWA. Exploiting a 20dB isolation between the two ends of the antennas, the other ports of the two LWAs are integrated with a 360-to-400GHz RX. For the RX, the output of the antenna is first converted to a differential signal through a rat-race balun followed by a double-balanced passive mixer. The LO to the mixer (greater than -10dBm across 360 to 400GHz) is generated in a similar manner as that of the TX chain. The IF output of the mixer is then fed to an IF amplifier with a simulated gain of 16dB with a bandwidth of 15GHz. The passive mixer has an overall double-sideband RX noise figure (NF) of 18.1dB.

To allow unique spectrum-to-space mapping, we avoid the use of a multi-frequency MIMO array by exploiting the frequency-dependent beam-pointing abilities of frequency-diverse surfaces. In this work, we employ two compact, moderate gain, wideband, on-chip LWAs. When a broadband pulse or a chirp is injected into such an antenna, the lower part of the spectrum radiates along the broadside and the higher part in an end-fire fashion (Fig. 22.1.1). However, for the system characterization we inject single tones to the chip and measure the performance at discrete frequencies. This feature is exploited to create a frequency-dependent spatial map response, which forms the basis vector to enable spatial localization of the mobile wireless nodes. By computationally analyzing a single spectral response from an unknown wireless link, one can enable link discovery techniques in a fast and effective manner without the need for scanning or mapping the 2D space. Dual on-chip LWAs enable 1D hemispherical coverage of the space. Further, two such orthogonally placed chips potentially enable 2D hemispherical coverage.

The design of the on-chip 360-to-400GHz LWA is shown in Fig. 22.1.3. The on-chip LWA antenna consists of a periodic slot array with a spacing of 43μm and an overall

length of 1.7mm. LWA waveguide width is chosen to be 225μm which corresponds to TE(1,0)- mode cut-off frequency of 320GHz. The LWA width, length, and the periodic slot spacing govern the dispersion relationship and support only positive propagating vectors, thereby covering the positive quadrant of the hemisphere. Though one could design the LWA to support the negative propagating vectors (composite left-handed material), these are extremely susceptible to losses. To cover the other quadrant, we enable another LWA which is fed from the opposite end with another dedicated TX. The simulated maximum gain of the LWA is 4.5dBi at 378GHz with a radiation efficiency of 19.3%. The LWA has fan-beam radiation patterns, with lower frequencies pointing close to broadside and higher frequencies to 40° . The LWA supports linear polarization and is oriented parallel to the direction of periodic slots. Exploiting a ~20dB isolation of the two LWA end-ports, a single antenna is interfaced with a TX and an RX at its two ends. Therefore, each IC can be configured to support three different modes of operation for link discovery, namely: transmitter-only mode, receiver-only mode, and full-duplex transceiver mode covering a frequency range of 360 to 400GHz. The measured radiation patterns and the frequency-dependent beam maxima in Fig. 22.1.3 demonstrate the key principle behind the proposed direction-finding. Measured co-to-cross polarization ratio is about ~18dB and the measured EIRP of the transmitter at 378GHz is -6.4dBm. The complete RX chain average NF with the antenna is measured to be ~26.2dB at the operating band. (Fig. 22.1.3).

To enable 1D direction-of-arrival (DOA) estimation, the spectrum to angular map is shown in Fig. 22.1.4, which captures the frequency-dependent radiation patterns (Fig. 22.1.3). Since the system is deterministic, given a spectrum from an unknown angle, we perform a correlation with this map and estimate the values that maximize the correlation. The number of frequency samples required to determine the basis calibration map is determined by the dispersion curve of the LWA as shown in Fig. 22.1.3. We show the angle-of-arrival error as a function of measurement RBW of the IF sampled signal. As shown in Fig. 22.1.4, the system along with our algorithm has a DoA estimation error of 0.95° for measurement RBW of 200Hz. With faster localization at RBW=20kHz, the DoA estimation error is about 2.1°. Measurements are performed using WR9.0 signal generation extension (SGX) followed by a WR4.3 frequency doubler and a WR2.2 second harmonic mixer that acts as an external TX or RX.

We also perform 2D DoA estimation using two orthogonal TX chips transmitting slightly different frequencies (1kHz offset). Similar to 1D localization, we create 2D frequency-to-space calibration maps that allow to perform 2D localization. We show the measured error in angle estimation and corresponding θ and ϕ error in Fig. 22.1.5. The measured 2D angle accuracy is $\sigma_\phi = 1.9^\circ$ and $\sigma_\Theta = 1.95^\circ$ for a measurement RBW of 20Hz. The functionality of 1D DoA estimation is also demonstrated between a TX and an RX enabled chip and is also shown in Fig. 22.1.5. Though the localization of nodes is shown in TX mode, the RX mode of localization is the same due to system reciprocity. The comparison table in Fig. 22.1.6 demonstrates the state-of-the-art performance. The die micrograph and the experimental setups are shown in Fig. 22.1.7.

Acknowledgement:

The authors would like to thank the Office of Naval Research, the Air Force Office of Scientific Research, the MURI Program, and the DURIP program for funding support. Authors also thank the IMRL members and John Suarez, U.S. Army CCDC C5ISR for technical discussions.

References:

- [1] Yasaman Ghasempour et al., "Single-Shot Link Discovery for Terahertz Wireless Networks," *Nature Comm.* 11.1 (2020): 1-6.
- [2] Hironori Matsumoto et al., "Integrated Terahertz Radar Based on Leaky-Wave Coherence Tomography," *Nature Elect.* 3.2 (2020): 122-129.
- [3] Haitham Hassanieh et al., "Fast Millimeter Wave Beam Alignment." *ACM SIGCOMM*. 2018.
- [4] Xiang Yi et al. "A Terahertz FMCW Comb Radar in 65nm CMOS with 100GHz Bandwidth," *ISSCC*, pp. 90-92, 2020.
- [5] Jidan Al-Eryani et al., "Fully Integrated Single-Chip 305–375-Ghz Transceiver with On-Chip Antennas in SiGe BiCMOS," *IEEE Trans. Terahertz Sci. Technol.*, vol. 8, no. 3, pp. 329-339, 2018.
- [6] Kaushik Sengupta et al., "Terahertz Integrated Electronic and Hybrid Electronic-Photonic Systems," *Nature Elect.* 1.12 (2018): 622-635.
- [7] Suresh Venkatesh et al., "A High-Speed Programmable and Scalable Terahertz Holographic Metasurface Based on Tiled CMOS Chips," *Nature Elect.*, In Press.
- [8] Xue Wu et al., "Programmable Terahertz Chip-Scale Sensing Interface with Direct Digital Reconfiguration at Sub-Wavelength Scales," *Nature Comm.* 10.1 (2019): 1-13.
- [9] Hooman Saeidi et al., "29.9 A 4x4 Distributed Multi-Layer Oscillator Network for Harmonic Injection and THz Beamforming with 14dBm EIRP at 416GHz in a Lensless 65nm CMOS IC," *ISSCC*, pp. 456-457, Feb. 2020.
- [10] Suresh Venkatesh et al., "Interferometric Direction Finding with a Metamaterial Detector." *Applied Physics Letters* 103.25 (2013): 254103.

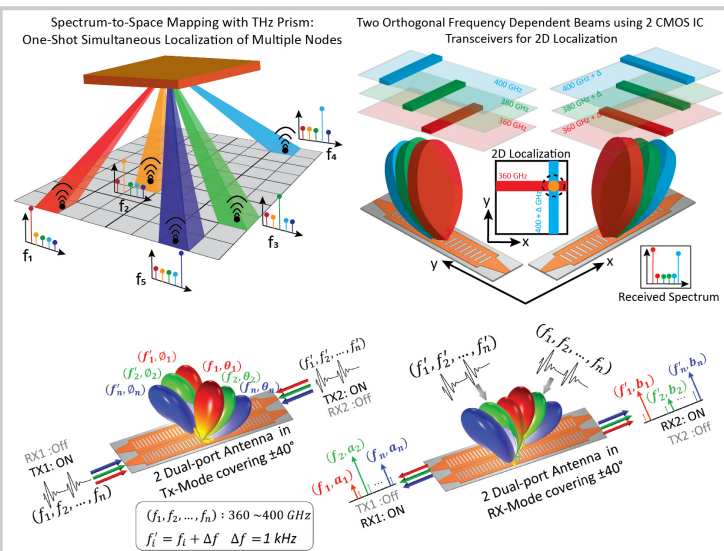


Figure 22.1.1: Concept of Spectrum-to-Space mapping with the THz Prism. Simultaneous and one-shot detection of multiple wireless nodes using frequency-diverse leaky-wave antennas is shown.

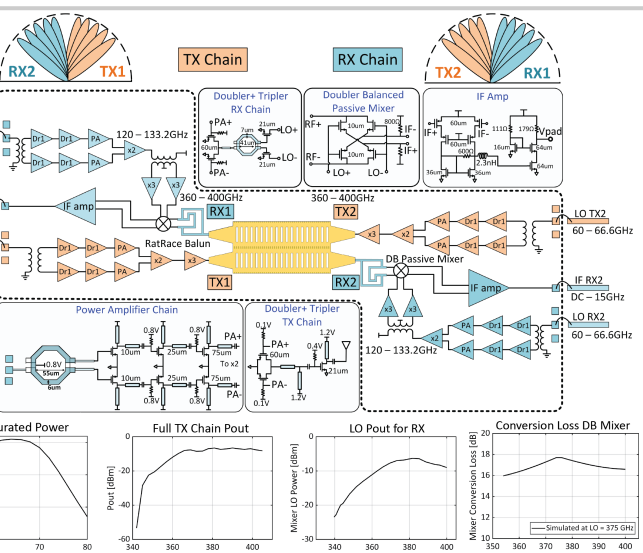


Figure 22.1.2: Broadband 360-to-400GHz transceiver architecture with two dual-port on-chip LWAs and the corresponding block simulation results.

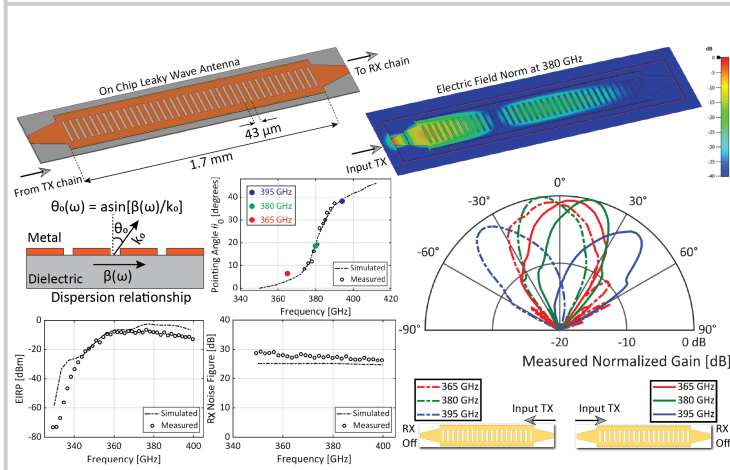


Figure 22.1.3: LWA design and TX/RX characterizations. Measured antenna beam patterns are shown for two on-chip TXs excited from opposite directions. Beam pointing angles vary from broadside to $\pm 40^\circ$ (solid line) and $\pm 40^\circ$ (dashed lines) when excited from left and right feed points respectively. The simulated and measured EIRP and NF of the TX and RX are also plotted.

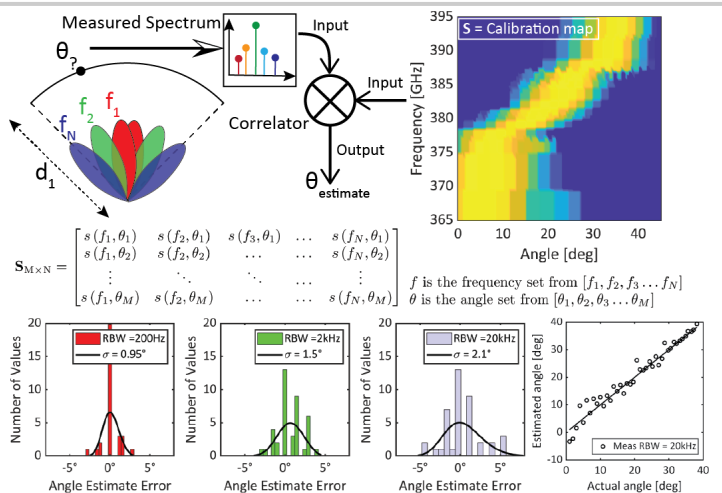


Figure 22.1.4: Concept and measurement performance of 1D angular localization using one CMOS IC. The antenna response as a function of frequency versus angle forms the basis calibration matrix S . The estimated angle and the standard deviations are shown for different measurement RBWs for randomized node locations.

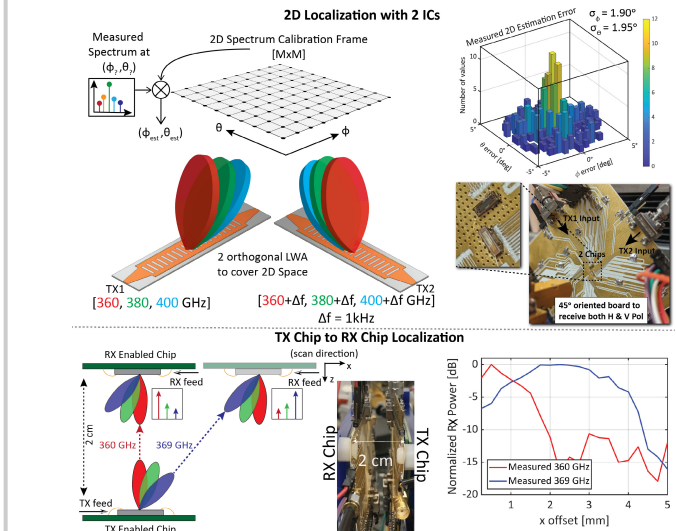


Figure 22.1.5: 2D Localization concept with two orthogonally placed chips shows angular error of 1.9° and 1.95° in the two orthogonal axes. Chip-to-chip localization is also demonstrated.

Metrics	This work	Nature Electr., '20 [2]	Nature Comm., '20 [1]	ISSCC '20 [4]	TTST '18 [5]
Architecture	TX/RX + OnchipAnt	TX/RX Dual off Chip Zero Bias detector + Dual off Chip LWA + Ext AMC	THz-TDS with fiber-coupled photoconductive antennas as source	TX/RX FMCW comb radar with 5 on chip multimode SiW antenna	TX/RX with On-Chip Patch antenna
Antenna Type	Periodic Leaky Wave	Uniform Leaky Wave waveguide	Uniform LWA (parallel plate waveguide)	multimode SiW antenna	Differential Patch Antenna
Frequency Range [GHz]	360 – 400	330 – 490	150 – 750	220 – 320	300 – 375
Prad per unit [dBm]	-10.9	-5 (off chip active x chain)	NA	0.6	3
Rx Noise Figure [dB]	26.2 (DSB avg)	NA	NA	22.2 DSB (min)	31.5 DSB avg (19.75 min)
Beam Coverage [deg]	-40 to +40	-51 to +51	+10 to +80	NA	NA
DoA Accuracy [deg]	± 0.95 (1D RBW = 200Hz) ± 1.9 (2D RBW = 20Hz)	± 5	± 5	NA	NA
Full Duplex operation	Yes	No	No	No	No
Power DC per Tx/Rx	TX 138mW RX 163mW	NA (off chip components)	NA (off chip components)	840mW Total	TX 568mW RX 751mW
Area [mm ²]	3	NA	NA	5	2.85
Technology	65nm CMOS	GaAs Schottky barrier ZBD with waveguide components	Off-the-shelf THz spectrometer components	65nm CMOS	130nm SiGe

Figure 22.1.6: Performance comparison with prior art in THz localizers and transceivers.

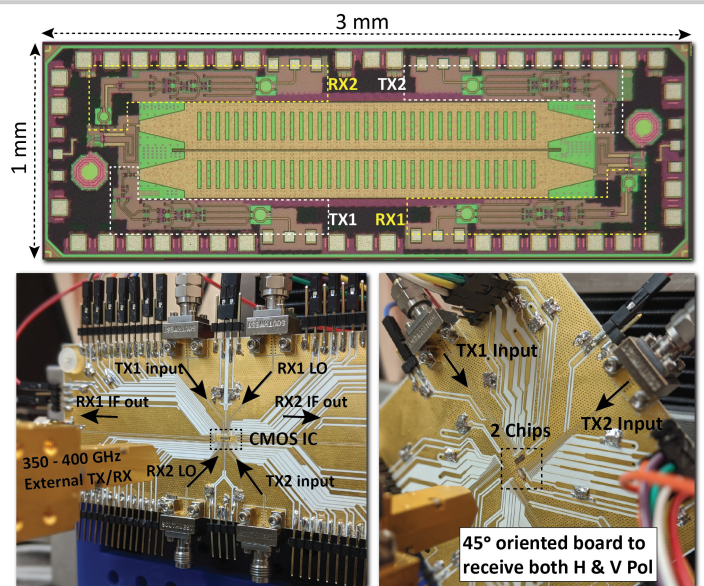


Figure 22.1.7: Fabricated die micrograph and experimental setups.

22.2 A 300GHz-Band Phased-Array Transceiver Using Bi-Directional Outphasing and Hartley Architecture in 65nm CMOS

Ibrahim Abdo¹, Carrel da Gomez¹, Chun Wang¹, Kota Hatano¹, Qi Li¹, Chenxin Liu¹, Kiyoshi Yanagisawa¹, Ashbir Aviat Fadila¹, Jian Pang¹, Hiroshi Hamada², Hideyuki Nosaka², Atsushi Shirane¹, Kenichi Okada¹

¹Tokyo Institute of Technology, Tokyo, Japan

²NTT, Kanagawa, Japan

This paper presents a CMOS bi-directional phased-array transceiver that covers the frequency range from 242 to 280GHz. The array consists of 4 elements with beamforming ability in the H-plane of the on-PCB Vivaldi antennas. The LO phase-generation scheme enables two different architectures for TX and RX modes. The TX mode utilizes an outphasing architecture while the Hartley architecture is adopted in the RX mode. The maximum achieved baud rates in the TX mode and the RX mode are 26Gbaud and 18Gbaud, respectively.

Achieving wireless communication using CMOS at frequencies around 250GHz and above is very challenging, considering the limited f_{max} of the CMOS transistors. Prior works adopted multiplier- or mixer-last transmitter topologies, as illustrated in Fig. 22.2.1. The multiplier-last topologies result in deformed constellations for the high-order modulation schemes, making it challenging to achieve higher data rates [1]. Mixer-last topology requires a very linear mixer to satisfy the SNDR requirements as the average output power is generally 6dB (power back-off, PBO) lower than the OP_{1dB} point [2]. Power combining results in higher total output power, but the power back-off is still needed making the actual output power much lower than the saturated output power [3-5]. All the mentioned prior works have line-of-sight (LoS) links as they depend mainly on a single-element transceiver and a high antenna-gain combination. Another issue is that the receivers are also designed separately, causing the system area to be quite large. To solve the problems of the conventional designs, the TX in this work utilizes the outphasing architecture. In addition, a passive subharmonic mixer similar to that in [2] is used to enable a bi-directional operation. The RX mode is based on Hartley architecture. The TX output power is further improved by implementing an end-fire 4-element phased array with wideband on-PCB Vivaldi antennas while providing beamforming ability.

Outphasing is usually used to improve the efficiency of power amplifiers by enabling the operation at output powers near the OP_{1dB} point. In this work, outphasing is used to increase the TX output power by operating the mixers at their saturated output power, as shown in Fig. 22.2.1. The average output power of the TX is comparable to that of the power-combining TXs as the back-off is not needed anymore. A 90° phase shift between the input LO signals is applied to cancel the LO feedthrough (LOFT) at the output. An additional 180° shift between the outphasing inputs (S1, S2) is required to recover the desired output. The two mixers are also used to downconvert the received signal with image cancellation, as illustrated in Fig. 22.2.1. The phase difference between the LO inputs in the RX case is 45°, which translates into the required 90° after the doubling of the subharmonic mixer. An additional 90° shift is applied externally at the output to reject the image signal coming from the TX.

Figure 22.2.2 shows the phased-array system architecture. Four elements with wideband Vivaldi antennas are stacked vertically, considering the short wavelength of the target frequency band. The circuit consists of two subharmonic passive mixers and two bi-directional IF distributed amplifiers in the signal path. The LO chain consists of three phase shifters, two frequency quadruplers, and LO buffers. The IF signal center frequency is 16GHz, and the LO input frequency is 30GHz. The LO frequency is multiplied by 4 to generate the 120GHz LO_{1/2} signal. Due to the subharmonic operation of the mixer, the IF signal is up- or down-converted by 240GHz. Thanks to the wide bandwidth of the IF distributed amplifier the resulting RF signal covers a 38GHz bandwidth from 242 to 280GHz. The circuit schematic of the IF amplifier connected to the mixer is shown in Fig. 22.2.2. The distributed bi-directional amplifier circuit is used to provide a wide bandwidth at the low center frequency. A simple cascode gain cell is used to build the amplifier. The mixer is based on the push-push doubler circuit as in [2]. The 1V bias at the output of the mixer improves the output power and the conversion gain as the parasitic capacitance between the source/drain and the bulk drops due to the high reverse bias. The improvement of the output power in the TX case is shown in Fig. 22.2.2. The observed improvement at the output is around 1dB.

The LO phase generation differs between TX mode and RX mode. The LO chain schematic is illustrated in Fig. 22.2.3. The first phase shifter has a 45° coverage and it sets the total LO phase to control the beam direction of the phased array. The next two phase shifters provide the required 90° and 45° LO phase shifts between the two mixers to enable the outphasing TX mode and the Hartley RX mode, respectively. The quadruplers extend the 45° range to 180°, which translates to a full 360° range at the subharmonic mixer output. The measured phase-shifter coverage at 30GHz is shown in Fig. 22.2.3. 120GHz LO buffers are designed for higher gain and output power by adding a positive feedback path for the single-ended stages, and by applying neutralization for the differential stages.

The phased array was implemented by stacking 4 PCBs with Liquid Crystal Polymer (LCP, $\epsilon_r=3$) flexible substrate. The spacing between every two elements is around 0.7mm (close to $\lambda/2$ at f_{center}). A part of the PCB is left flexible to fit the connectors. The flip-chip process is used to connect the CMOS die to the PCB. IF and LO signals are amplified and split externally. The H-plane radiation patterns of the array are shown in Fig. 22.2.3.

The single-element LO emission-cancellation technique is illustrated in Fig. 22.2.4. The doubler-based mixer results in a LOFT with twice the frequency of the input LO. Hence, providing a 90° phase shift between the two mixers results in canceling the LOFT at the TX output (or RX input). The measured cancellation exceeds 30dB in both TX and RX modes. The other RX mode (Hartley architecture) provides more than 40dB image cancellation as shown in Fig. 22.2.4. The image was observed by slightly shifting the downconversion frequency.

Figure 22.2.5 shows the performance summary and the constellations of the 1-element TX mode. 52Gb/s maximum data rate is achieved by using QPSK. The maximum 16-QAM data rate is 48Gb/s. The IEEE802.15.3d standard constellations are also measured and the constellations are shown in Fig. 22.2.5. For TX-to-RX OTA measurement, TX and RX are connected to 26dBi antennas through waveguide probes over a 2.5cm distance. 16Gb/s is the maximum measured data rate of the 1-element TRX. The TRX consumes around 750mW DC power for both TX mode and RX mode.

Figure 22.2.6 shows a comparison between this work and the other state-of-the-art CMOS 200-to-300GHz transceivers. Figure 22.2.7 shows the die micrograph of the TRX, which was fabricated in a 65nm CMOS process. The total chip area is 4.17mm².

Acknowledgement:

This work is partially supported by STAR, and VDEC in collaboration with Cadence Design Systems, Inc., Synopsys Inc., Mentor Graphics, Inc., and Keysight Technologies Japan, Ltd.

References:

- [1] S. Kang et al., "A 240 GHz Fully Integrated Wideband QPSK Transmitter in 65 nm CMOS," *IEEE JSSC*, vol. 50, no. 10, pp. 2256-2267, Oct. 2015.
- [2] I. Abdo et al., "A 300GHz Wireless Transceiver in 65nm CMOS for IEEE802.15.3d Using Push-Push Subharmonic Mixer," *IEEE IMS*, pp. 623-626, June 2020.
- [3] K. Takano et al., "A 105Gb/s 300GHz CMOS transmitter," *ISSCC*, pp.308-309, Feb. 2017.
- [4] S. Hara et al., "A 32Gb/s 16QAM CMOS Receiver in 300GHz Band," *IEEE IMS*, pp. 1703-1706, June 2017.
- [5] S. Lee et al., "An 80-Gb/s 300-GHz-Band Single-Chip CMOS Transceiver," *IEEE JSSC*, vol. 54, no. 12, pp. 3577-3588, Dec. 2019.
- [6] S. V. Thyagarajan et al., "A 240 GHz Fully Integrated Wideband QPSK Receiver in 65nm CMOS," *IEEE JSSC*, vol. 50, no. 10, pp. 2268-2280, Oct. 2015.
- [7] M. Cho et al., "A Switchless CMOS Bi-Directional Distributed Gain Amplifier With Multi-Octave Bandwidth," *IEEE MWCL*, vol. 23, no. 11, pp. 611-613, Nov. 2013.
- [8] A. Standaert and P. Reynaert, "A 390-GHz Outphasing Transmitter in 28-nm CMOS," *IEEE JSSC*, vol. 55, no. 10, pp. 2703-2713, Oct. 2020.

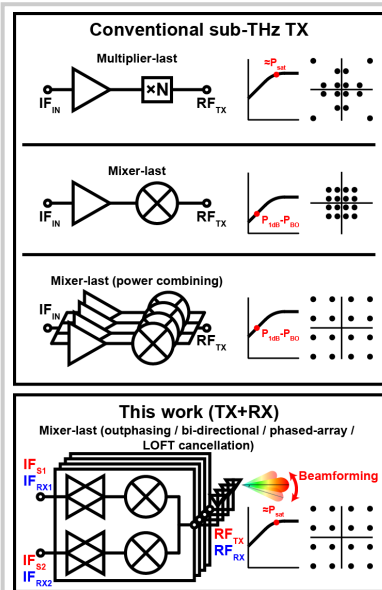


Figure 22.2.1: Architecture of proposed sub-THz phased-array transceiver.

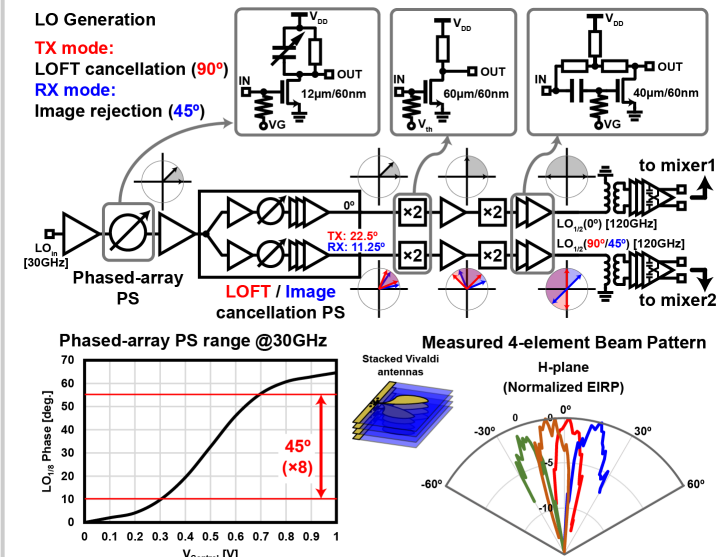


Figure 22.2.3: Phase-shifter chain, measured phase coverage and radiation pattern.

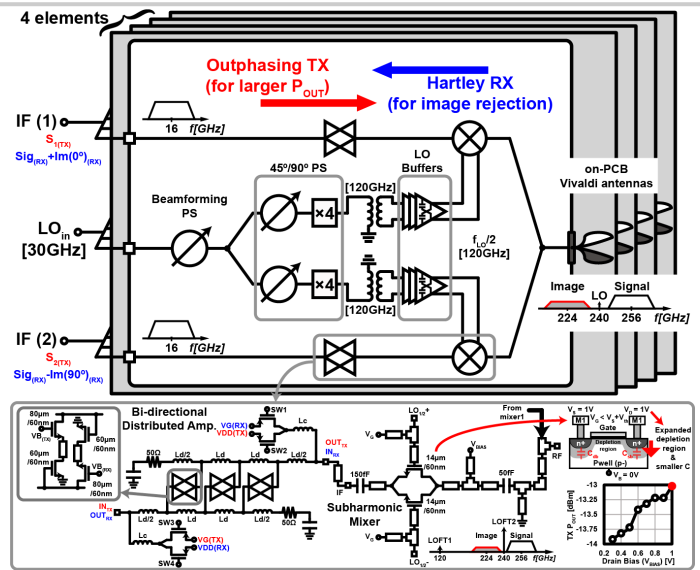


Figure 22.2.2: Block diagram of 300GHz-band CMOS bi-directional phased-array TRX system.

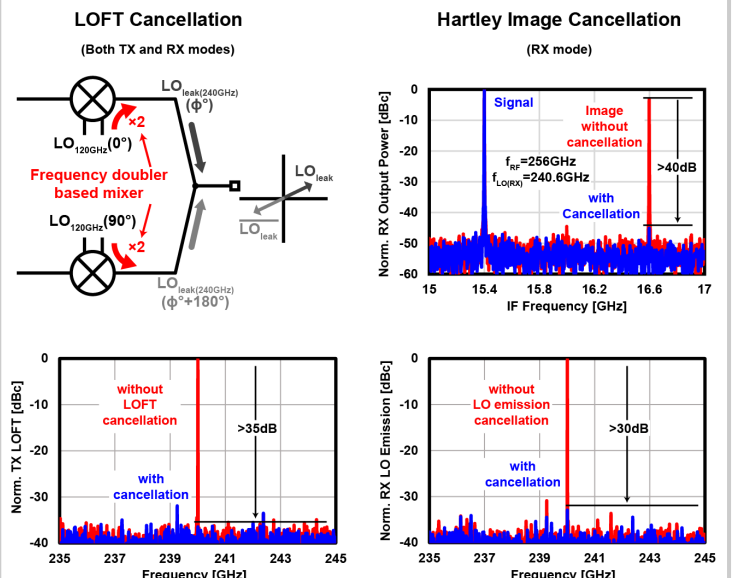


Figure 22.2.4: Measured characteristics for TX and RX modes.

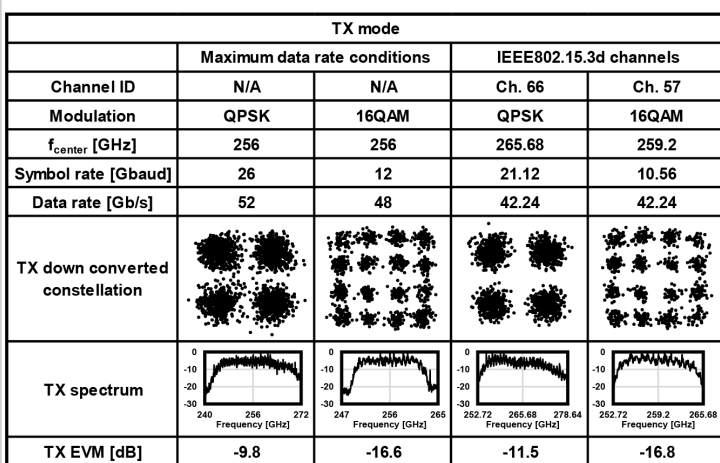


Figure 22.2.5: Measured constellations and performance summary in TX mode.

	[1],[6]	[3],[4]	[5]	[2]	This work
Tech. [nm]	65 CMOS	40 CMOS	40 CMOS	65 CMOS	65 CMOS
RF freq. [GHz]	240*	290*	252-279	278-304	242-280
Structure	Single-element	Single-element	Single-element	Single-element	Phased array
Architecture	Uni-directional	Uni-directional	Uni-directional	Uni-directional	Bi-directional
TX topology	Single stream tripler-last	Power combining	Power combining	Single stream mixer-last	Outphasing +Hartley
Max. baud rate [Gbaud]	TX: 8 RX: 8	TX: 21 RX: 14	TX: 28 RX: N/A	17	TX: 26 RX: 18
P _{DC} [W]	TX: 0.22 RX: 0.26	TX: 1.4 RX: 0.65	TX: 0.89 RX: 0.9	TX: 0.27 RX: 0.14	TX: 0.75 RX: 0.75
Area [mm ²]	TX: 2 RX: 2	TX: 5.19 RX: 3.15	TRX: 11	TX: 1.9 RX: 1.9	TRX: 4.17

*Center frequency

Figure 22.2.6: Performance comparison with state-of-the-art 300GHz-band transceivers.

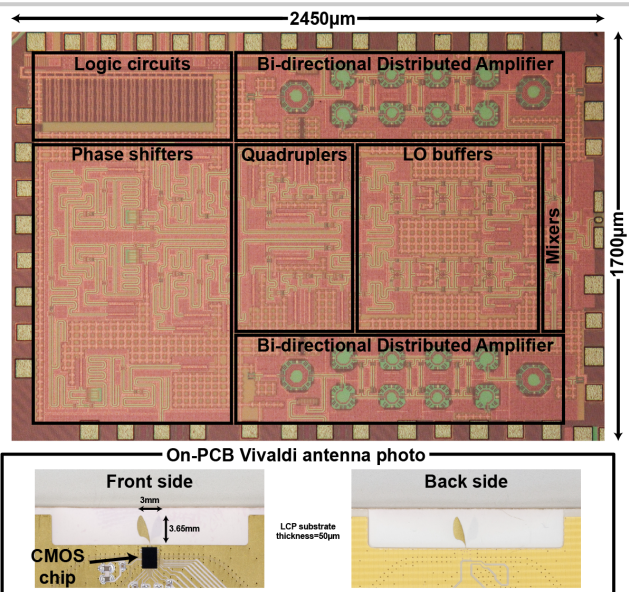


Figure 22.2.7: Die micrograph and on-PCB antenna photos.

22.3 A 0.42THz Coherent TX-RX System Achieving 10dBm EIRP and 27dB NF in 40nm CMOS for Phase-Contrast Imaging

Dragan Simic, Kaizhe Guo, Patrick Reynaert

KU Leuven - MICAS, Leuven, Belgium

The small wavelength and non-ionizing nature of EM waves in the THz spectrum make this frequency band attractive for high-resolution imaging applications. While amplitude-based THz imaging systems have already been demonstrated in Silicon [1], an integrated solution for phase detection in this frequency range has not been reported so far. Detecting the phase change of THz waves passing through the imaged object would enable applications like high-precision thickness measurement and dielectric permittivity characterization. Furthermore, phase-contrast imaging techniques allow scanning of weakly absorbing materials, such as soft tissues and polymers, where amplitude-based scanners are incapable of providing clear pictures [2]. However, the mentioned applications demand high phase-detection accuracy, imposing strict SNR requirements on THz phase imagers for real-time operation. The main SNR limitation of such systems comes from the high NF of the THz receivers [3,4], due to the lack of an LNA prior to downconversion of the THz signal. This paper proposes a two-step IQ downconversion RX architecture with low-loss LO power combining as a way to alleviate the mentioned problem, achieving RX NF of 27dB at 420GHz. Additionally, it presents a frequency-locked TX that achieves 10dBm EIRP, leading to 52dB SNR (100kHz RBW) of the TX-RX coherent imaging system when operating at a distance of 25cm. This system demonstrates 420GHz phase detection with RMS accuracy of 2.8° and RMS 1σ precision of 1.7°.

Figure 22.3.1 illustrates the presented imaging system, together with schematics of the designed chips. The proposed two-step IQ downconversion RX architecture lowers the LO frequency of the first mixer, which facilitates high-power LO generation, while preserving fundamental mixing operation. A four-stage LNA follows the first mixer, minimizing the impact of the second mixer on the overall NF. The LO generation for both mixers starts from a 17.5GHz (f_{REF}) external reference and consists of a multiplier-buffer chain, creating 315GHz (18× f_{REF}) and 105GHz (6× f_{REF}) references for the first and the second mixer, respectively. The TX uses the same off-chip reference for signal generation, establishing frequency synchronization between chips. The TX modulation is implemented to set the output frequency of the system above the RX 1/f noise corner, further increasing the overall SNR. The frequency planning of the multiplier chains used in the TX and the RX first mixer LO generation ensures negligible parasitic radiation of those blocks at the RX image (12× f_{REF}) and the first IF (6× f_{REF}) frequencies, thus avoiding possible phase-detection inaccuracies caused by TX or RX leaks.

The schematic and layout of the RX core is shown in Fig. 22.3.2. It consists of 157.5GHz (9× f_{REF}) to 315GHz (18× f_{REF}) doublers, a double-balanced passive mixer and a folded-dipole antenna. Two-way power combining is implemented to increase the limited first mixer LO power. The combining paths are routed to opposite mixer sides, thus fully exploiting the area around the mixer and decreasing the distance between the mixer and doublers. This reduces the loss caused by long THz interconnections and makes the mixer layout fully symmetrical. The matching baluns between the mixer and doublers are designed using transformers. The transformer center taps are AC-shorted to doubler grounds at 315GHz through series LC resonators, facilitating mixer biasing and ensuring balance of the LO signals. The mentioned techniques result in simulated mixer insertion loss of 10.8dB. Combined with 49% simulated antenna efficiency and 10.1dB NF of the LNA together with the second mixer this gives a total simulated RX NF of 24dB.

Figure 22.3.3 shows schematic and layout of the TX core. It consists of a 140GHz (8× f_{REF}) to 420GHz (24× f_{REF}) tripler and a folded-dipole antenna. The tripler is implemented as a pseudo-differential NMOS pair with cross-coupling capacitors between input and output. Load impedances of the tripler at the first three harmonic frequencies are optimized to enhance the third-harmonic generation. While driven by 9.6dBm power at 140GHz, the simulated third-harmonic output power is -5.3dBm. This combined with a simulated antenna efficiency of 44% results in a TX radiated power of -8.9dBm. The TX modulation is implemented by mixing the TX signal with a (1,-1) modulation signal, resulting in 90% of the TX output power contained in the 24× f_{REF} - f_{MOD} and 24× f_{REF} + f_{MOD} tones. This presents 5.4dB signal improvement compared to the commonly used (1,0) output chopping.

The die micrographs of the fabricated 40nm bulk CMOS chips are shown in Fig. 22.3.7. The RX and TX areas are 2.89mm² and 2mm², respectively. Hyper-hemispherical Silicon lenses ($D_{RX}=6mm$, $D_{TX}=5mm$) are used to increase directivity of the on-chip antennas. The RX and TX are characterized using VDI WR2.2 TX and RX modules, calibrated by a

PM5 power meter, both at a distance larger than 20cm. The measured directivities of the designed antennas at 420GHz are 20.5dBi and 19dBi, for the RX and TX respectively. Figure 22.3.4 shows the measurement results of the chips. The measured RX isotropic gain and NF at 420GHz are 41.5dB and 6.5dB, respectively. Together with the measured RX antenna directivity these result in 21dB conversion gain and 27dB NF at 420GHz. The measured TX EIRP at 420 GHz is 10dBm. Using the measured EIRP and TX antenna directivity, the TX radiated power at 420GHz is calculated as -9dBm. The measured power consumptions of the TX and RX chips, from a 1V supply, are 304mW and 601mW.

Figure 22.3.5 shows the phase-detection performance of the presented system at 420GHz. The imaging setup from Fig. 22.3.1 is used in this measurement, with the TX-RX distance of 25cm. The measured SNR at the RX outputs, with non-modulated transmitter, is 52dB (100kHz RBW). To test the phase-detection performance of the system a programmable external phase-shifter is inserted in the TX LO path, creating a 420GHz signal with 2.4° phase step at the TX output. Figure 22.3.5 is obtained by modulating the TX with a 10MHz signal and sweeping the TX output phase over 400° range. The RX output voltages are measured using an Agilent MSO9104A oscilloscope, without any filtering or averaging, with time span of only 500ns and sampling frequency of 10GS/s (FFT fbin=2MHz). To quantify accuracy and precision of the presented system this measurement is repeated 100 times. The RMS value of the phase detection accuracy over a range of 400° is 2.8°, with an RMS 1σ precision of 1.7°.

A practical example of THz phase imaging is shown in Fig. 22.3.6. Text is printed on a paper and placed between the presented chips. The attenuation of the ink is negligible, making the text reconstruction difficult with the amplitude detection alone. However, the dielectric properties of the ink create a phase shift at 420GHz which can be detected by the presented system. The image in Fig. 22.3.6 is obtained by mapping the measured phase on a gray-scale. The contrast between the image regions with and without the ink is strong enough for the text to be clearly recognized. In contrast, the amplitude image, obtained from the same measurement and using the same gray-scale mapping, hardly reveals any information. This demonstrates the added value of THz phase sensing for imaging and object detection. It should be noted that no signal processing, image enhancement or pixel correction is applied to obtain these raw images.

Figure 22.3.6 also compares the designed chips with the prior art of THz CMOS coherent receivers and frequency-locked radiating transmitters. The designed RX and TX achieve superior NF and EIRP, resulting in 52dB SNR (100kHz RBW) of the TX-RX system at 25cm distance. This system demonstrates the real-time phase imaging performance (500ns/pixel), achieving 2.8° RMS phase accuracy and 1.7° RMS 1σ precision above 300GHz in Silicon.

Acknowledgement:

The authors would like to acknowledge the EUROPRACTICE MPW and design tool support. Also, the authors would like to thank Hui Liu and Gabriel Guimaraes from KU Leuven MICAS group for assistance during the measurements.

References:

- [1] R. Jain et al., "A 0.42THz 9.2dBm 64-Pixel Source-Array SoC with Spatial Modulation Diversity for Computational Terahertz Imaging," *ISSCC*, pp. 440-441, Feb. 2020.
- [2] T. Davis et al., "Phase-Contrast Imaging of Weakly Absorbing Materials Using Hard X-Rays", *Nature*, vol.373, pp. 595-598, Feb. 1995.
- [3] Q. Zhong et al., "Terahertz RF Front-End Employing Even-Order Subharmonic MOS Symmetric Varactor Mixers in 65-nm CMOS for Hydration Measurements at 560GHz," *IEEE Symp. VLSI Circuits*, pp 211-212, June 2018.
- [4] K.-S. Choi et al., "A 490GHz 32mW Fully Integrated CMOS Receiver Adopting Dual-Locking FLL", *ISSCC*, pp. 452-453, Feb. 2020. [5] K. Guo et al., "A 0.53-THz Subharmonic Injection-Locked Phased Array With 63-uW Radiated Power in 40-nm CMOS," *IEEE JSSC*, vol. 54, no. 2, pp. 380-391, Feb. 2014.
- [6] T. Chi et al., "A Packaged 90-to-300GHz Transmitter and 115-to-325GHz Coherent Receiver in CMOS for Full-Band Continuous-Wave mm-Wave Hyperspectral Imaging," *ISSCC*, pp. 304-305, Feb. 2017.
- [7] Y. Yang et al., "An Eight-Element 370-410-GHz Phased-Array Transmitter in 45-nm CMOS SOI With Peak EIRP of 8-8.5 dBm," *IEEE TMTT*, vol. 64, no. 12, pp. 4241-4249, Dec. 2016.
- [8] F. Golcuk et al., "A 0.39-0.44 THz 2x4 Amplifier-Quadrupler Array with Peak EIRP of 3-4 dBm," *IEEE TMTT*, vol. 61, no. 12, pp. 4483- 4491, Dec. 2013.

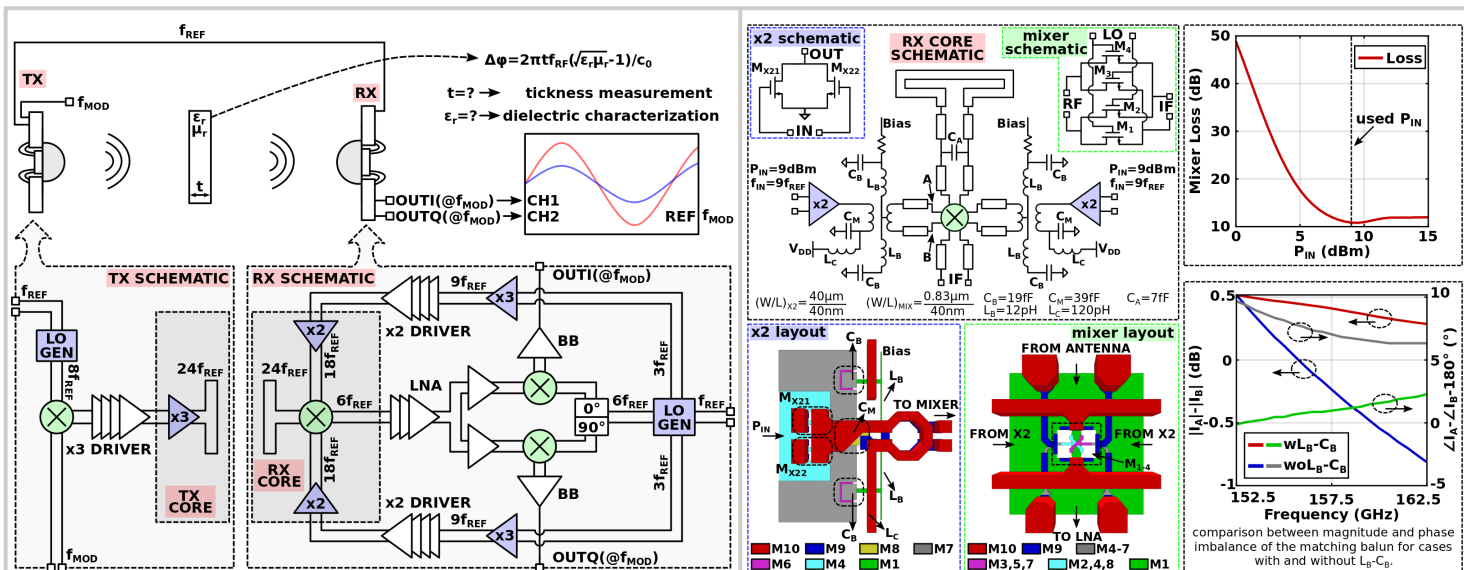


Figure 22.3.1: Illustration of the proposed phase imaging system, together with schematics of the designed chips.

Figure 22.3.2: Schematic and layout of the RX core (left). Mixer loss versus doubler input power and demonstration of the L_B-C_B balancing technique (right).

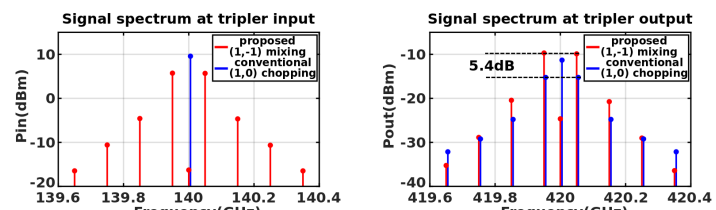
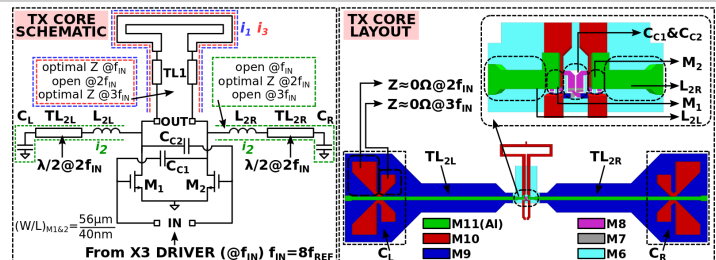


Figure 22.3.3: Schematic and layout of the TX core (top). Spectra at input and output of the tripler in cases of the proposed modulation (1,-1) and the conventional chopping (1,0) (bottom).

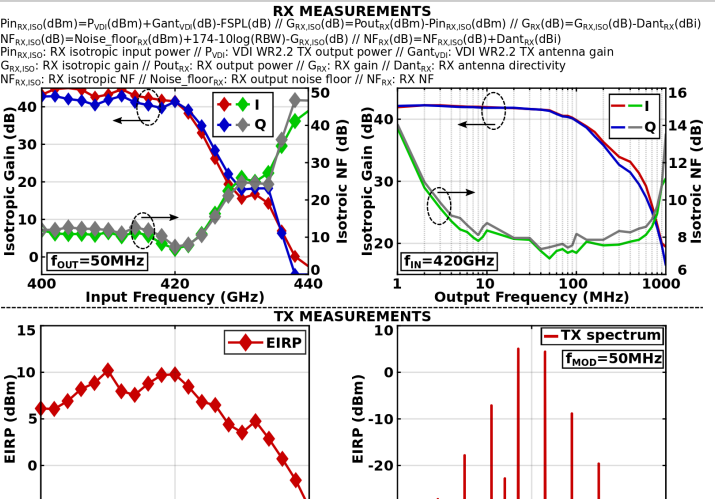


Figure 22.3.4: The measured RX isotropic gain and NF versus input and output frequency (top). The measured non-modulated TX EIRP versus frequency and the measured modulated TX spectrum, for f_{MOD} of 50MHz (bottom).

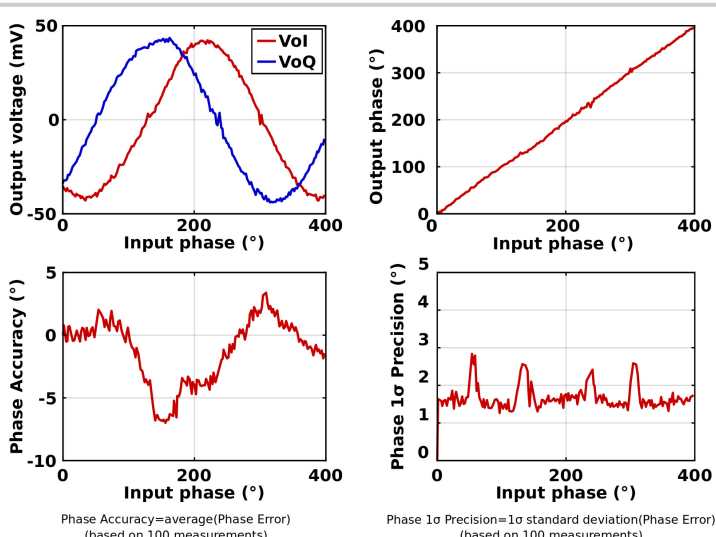


Figure 22.3.5: Example of the measured RX output voltages and the phase detection, with the TX-RX distance of 25cm (top). The measured TX-RX phase accuracy and precision, based on 100 measurements (bottom).

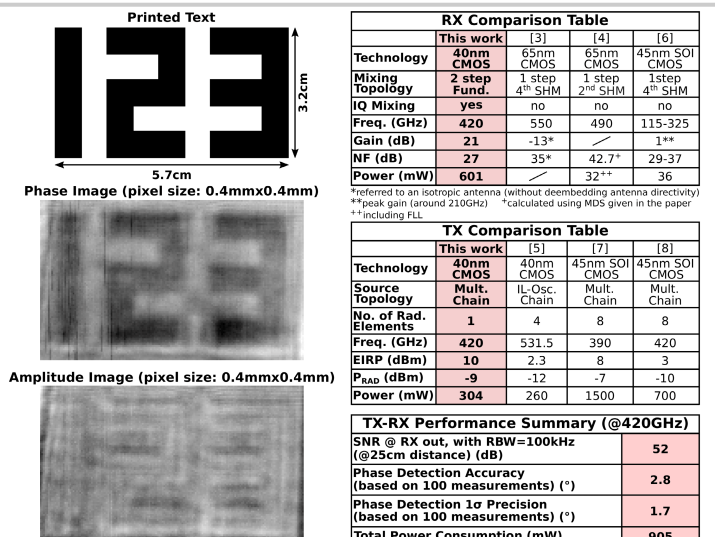


Figure 22.3.6: Phase imaging demonstration (left). Comparison of the designed chips with the state-of-the-art CMOS THz coherent receivers and frequency-locked transmitters, and TX-RX performance summary (right).

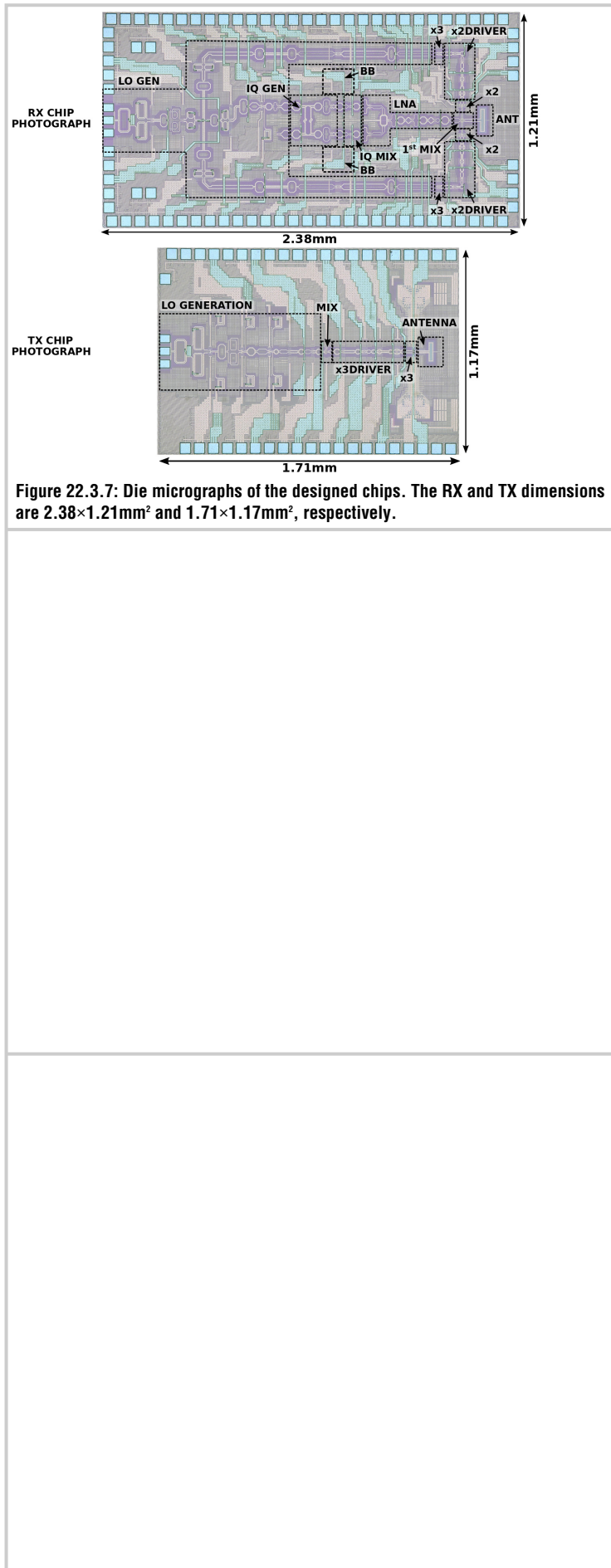


Figure 22.3.7: Die micrographs of the designed chips. The RX and TX dimensions are $2.38 \times 1.21\text{mm}^2$ and $1.71 \times 1.17\text{mm}^2$, respectively.

22.4 A 250GHz Autodyne FMCW Radar in 55nm BiCMOS with Micrometer Range Resolution

S. M. Hossein Naghavi¹, Saghar Seyedabbaszadehesfahlani¹, Farzad Khoeini¹, Andreia Cathelin², Ehsan Afshari¹

¹University of Michigan, Ann Arbor, MI

²STMicroelectronics, Crolles, France

The increasing demands for compact, low-cost, and high-resolution radar systems have pushed the operation frequency to the terahertz range due to the shorter wavelength and larger available bandwidth [1-5]. However, the best-reported range resolution cannot go below 1.5mm with a 100GHz bandwidth [1], which is not enough for many industrial applications like small-defect detection and surface screening. Moreover, most previous works [3-5] are based on conventional transceiver architectures that use separate antennas for TX and RX or use parallel multi-antenna designs to increase the frequency bandwidth [1]. These structures not only increase the chip size but also degrade the radar performance when they are placed at the focal point of a collimating lens. This degradation occurs due to the separated antenna phase centers, which are not well located at the collimating lens focal point, causing a multi-beam radiation pattern. To overcome these challenges, we have adopted an *autodyne* FMCW radar structure [6,7] with a phase processing method on the radar IF signal [7]. The autodyne is an oscillator that simultaneously carries out functions of generating the transmission and mixing the transmitted and reflected signals. There is no separate path for the RX signal in the autodyne, as the radiated and reflected signals exist at the same point of the autodyne circuit. Hence, it utilizes a combined antenna with a single-phase center for both transmitting and receiving parts. Besides, the phase processing method allows us to measure short ranges with an error no more than one-tenth of one-percent, which in terahertz frequencies provides micrometer resolutions [7]. Using these approaches, this paper demonstrates an autodyne FMCW radar with 66.7GHz bandwidth from 191GHz to 257.7GHz with a minimum range resolution of 54μm. Across state-of-the-art, this design improves the range resolution by 28 times.

Figure 22.4.1 reveals the block diagram of an FMCW radar imaging system with a phase processing method. In the conventional FMCW radars that use frequency processing, the range-resolution equation of $c/2B$ is achieved when the phase of the IF signal increases by 360°. However, with available FFT processors, reaching a phase resolution of 1° is feasible, which results in micrometer-range resolutions at THz frequencies. As shown in Fig. 22.4.1, some technical limitations prevent us from such level of accuracy. The first challenge is the instability at the start frequency (f_0) and bandwidth (Δf) of the radar chirp that causes an unpredictable phase variation at the IF. In FMCW radars that utilize harmonic oscillators to generate THz signals, this frequency instability is inherent. The second issue is the time delay between the start time for A/D sampling and the start time for the chirp signal, which is modeled by t_s in the discrete-time equation [8]. Even though a trigger signal synchronizes the A/D and ramp generator, there are still small time differences in the consecutive measurements that cannot be removed and cause random phase differences in IF signals. THz FMCW radars with a harmonic oscillator or frequency multiplier chain have this type of phase uncertainty. To stabilize the phase, one approach is to use a PLL, and the other one is to employ a calibration channel with determined delay to compensate for the phase variations in the processing domain. The calibration channel is shown as a reflection from a reference object in Fig. 22.4.1. The actual value of the phase deviation is measured through a calibration channel, and the appropriate correction is calculated.

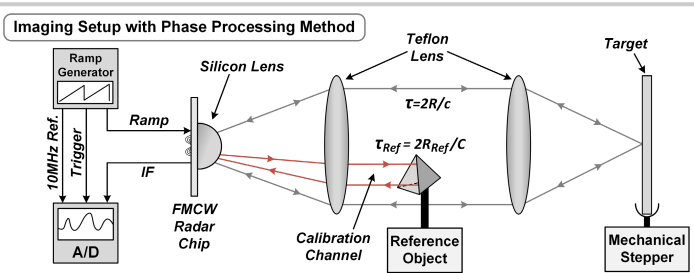
The schematic of the autodyne FMCW radar is shown in Fig. 22.4.2. To generate power around f_{max} , we designed a wideband VCO utilizing a harmonic Colpitts oscillator optimized for output power and tuning range based on the method presented in [3]. A pair of varactors C_i is used for frequency tuning, and they resonate with the lines T_1 at the base of Q_1 . Two kΩ resistors (R_{b1}, R_{b2}) at point V_b enforce VCO differential operation at the fundamental frequencies. Lines T_2 not only provide the optimum loading condition for maximum activity of Q_1 but also compensate the parasitic capacitors around Q_1 and greatly enhance the bandwidth of the Colpitts oscillator. Simulations and measurements verify a tuning range of 66.7GHz (29.7%) from 191 to 257.7GHz. Using a current reuse technique, Q_1 is buffered via Q_2 to boost generated second-harmonic power and isolate the VCO tank from the loading of output networks. A Double-Fed Capacitive-Loaded Slot (DFCLS) structure is a multifunctional EM structure for further improvement of VCO operation, which is made up of microstrip transmission lines (T_3), slot lines, and capacitor terminations (Cap). The DFCLS at the collectors of Q_2 acts as an optimum load at fundamental and second harmonics and functions as a wideband transmitting and receiving antenna. As illustrated in Fig. 22.4.2, at the fundamental frequency (f), the short-circuit plane returns almost the entire current to the structure and provides an

inductive loading (Z_{odd}) at Q_2 collectors. Due to the short-circuit plane, weak electric fields are excited in the slot lines and can be ignored in the Z_{odd} calculations. However, at the second harmonic ($2f$), the in-phase currents of Q_2 form an open-circuit plane at the center of the DFCLS. The entire second-harmonic currents are injected into the slot lines and excite an in-phase strong E-field. The values of capacitor termination (Cap), length, and impedance of slot lines are optimized in combination with lines T_3 to provide the optimum loading at the second harmonic Z_{even} for Q_2 collectors. In simulations, the maximum power of 3dBm is delivered to the DFCLS. A $\lambda/4$ line after the DFCLS prevents the leakage of the second harmonic to the V_{cc} port. The full-wave simulated radiation pattern of the DFCLS with a high-resistivity Si (HR-Si) lens is demonstrated in Fig. 22.4.3, which has a 31% antenna efficiency and 18.9dBi directivity at 220GHz. In the mixer mode, the input wave at $2f + f_F$ is coupled into the heavily driven Q_2 transistors via the DFCLS receiving antenna. Both the input signal and the LO signal at $2f$ are in common mode, which enables the extraction of the combined, downconverted signal f_F through the V_{cc} port. Simulations show that the nonlinearities of CB junctions of Q_2 mainly perform the mixing process; hence, the mixer and oscillator parts are isolated, which improves the system performance.

The chip was characterized using a VDI Erikson PM4 power meter and two FS-Z220 and FS-Z325 Rohde&Schwarz harmonic mixers. The chip EIRP is shown in Fig. 22.4.4 with a maximum EIRP of 17dBm, and EIRP variations of 6.5dB. The antenna radiation patterns at E and H planes are plotted in separate figures to show the radiation pattern consistency. They show that the antenna phase center in the entire band remains at the silicon lens center. The total performance of the FMCW radars can be somehow related to the received power fluctuations at the IF signal because it includes the collected effects of TX power variations, antenna pattern fluctuations, and RX conversion-gain variations over the band. Figure 22.4.4 shows a 10.4dB measured received power variation of the chip when placed in front of a collimating Teflon lens and a calibrating corner reflector. To determine the range resolution of radar using the phase processing method, a measurement setup (Fig. 22.4.5) was used with a Thorlabs DDS300 direct-drive translation stage. The uncertainty of range measurement at different positions was calculated by repeating each measurement 50 times. The error bars in Fig. 22.4.5 show $\pm 2\sigma$, which is equivalent to 95.5% confidence. The measured range errors W and W/O averaging are better than 0.015% and 0.025%, respectively. Figure 22.4.6 also shows two THz images illustrating the radar capability for resolving 70μm steps on flat aluminum surfaces. The die micrograph of the IC is shown in Fig. 22.4.7. It has an area of 0.22mm² and consumes 68mW of power.

References:

- [1] X. Yi et al., "A Terahertz FMCW Comb Radar in 65nm CMOS with 100GHz Bandwidth," *ISSCC*, pp. 90-92, Feb. 2020.
- [2] J. Grzyb et al., "A 210–270-GHz Circularly Polarized FMCW Radar with a Single-Lens-Coupled SiGe HBT Chip," *IEEE Trans. THz Sci. Technol.*, vol. 6, no. 6, pp. 771-783, Nov. 2016.
- [3] A. Mostajeran et al., "A High-Resolution 220-GHz Ultra-Wideband Fully Integrated ISAR Imaging System," *IEEE TMTT*, vol. 67, no. 1, pp. 329-339, Jan. 2019.
- [4] A. Visweswaran et al., "A 145GHz FMCW-Radar Transceiver in 28nm CMOS," *ISSCC*, pp. 168-169, Feb. 2019.
- [5] J. Al-Eryani et al., "Fully Integrated Single-Chip 305–375-GHz Transceiver with On-Chip Antennas in SiGe BiCMOS," *IEEE Trans. THz Sci. Technol.*, vol. 8, no. 3, pp. 329-339, May 2018.
- [6] Y. H. Kao et al., "A Single-Port Duplex RF Front-End for X-Band Single-Antenna FMCW Radar in 65nm CMOS," *ISSCC*, pp. 318-319, Feb. 2017.
- [7] I. V. Komarov, and S. M. Smolskiy, *Fundamentals of Short-Range FM Radar*, Artech House, 2003.
- [8] B. Yektakhan et al., "All-Directions Through-The-Wall Imaging Using a Small Number of Moving Omnidirectional Bi-Static FMCW Transceivers," *IEEE Trans. Geosci. Remote Sens.*, vol. 57, no. 5, pp. 2618-2627, May 2019.



Phase Processing Method in FMCW Radars

1- FMCW TX and RX signals:

$$S_{TX}(t) = \exp(j(2\pi f_0 t + \pi\gamma t^2))$$

$$S_{RX}(t) = \exp(j(2\pi f_0(t-t_r) + \pi\gamma(t-t_r)^2))$$

2- Continuous-time FMCW IF signal:

$$S_{IF}(t) \approx \exp(j(2\pi f_0 t + 2\pi\gamma t))$$

3- Discrete-time FMCW IF signal (F_s : A/D sampling rate):

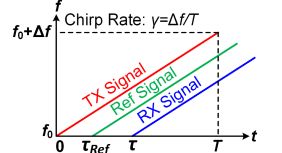
$$t = k/F_s + t_s$$

$$S_{IF}(k) \approx \exp(j(2\pi f_0 t + 2\pi\gamma t_s + 2\pi\gamma k/F_s))$$

4- Phase of IF and reference signals:

$$\phi_{IF} = 2\pi(f_0 + \gamma t_s)\tau$$

$$\phi_{Ref} = 2\pi(f_0 + \gamma t_s)\tau_{Ref}$$



5- Ratio of IF phase and reference phase:

$$\tau = \frac{\phi_{IF}}{\phi_{Ref}} \tau_{Ref}$$

Known values

$$R = \frac{\phi_{IF}}{\phi_{Ref}} R_{Ref}$$

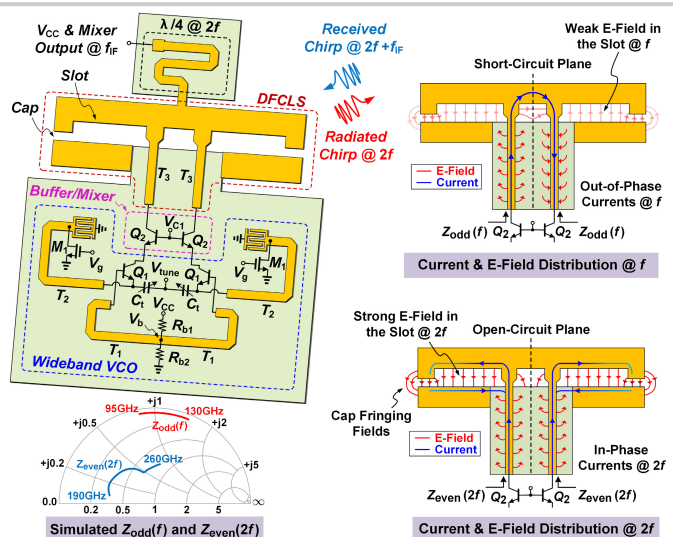


Figure 22.4.1: Imaging setup (top) and formulation (bottom) of the phase processing method in FMCW radars.

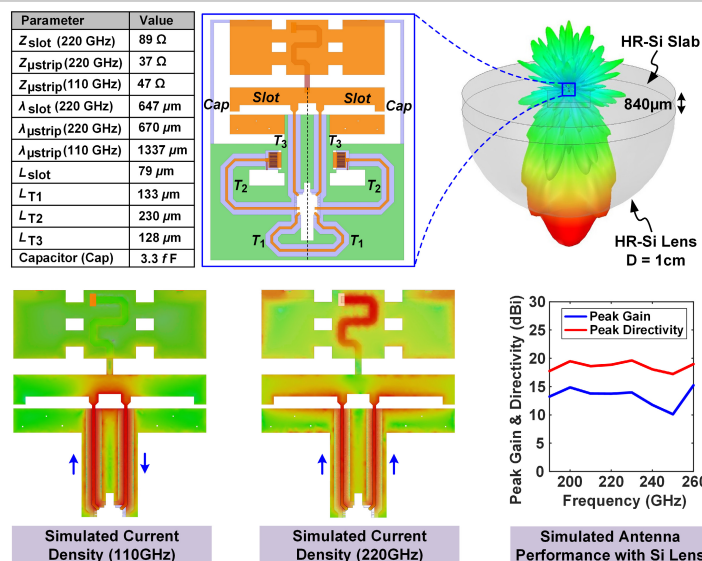


Figure 22.4.3: Structure and simulation results for DFCLS, and simulated antenna performance with HR-Si lens.

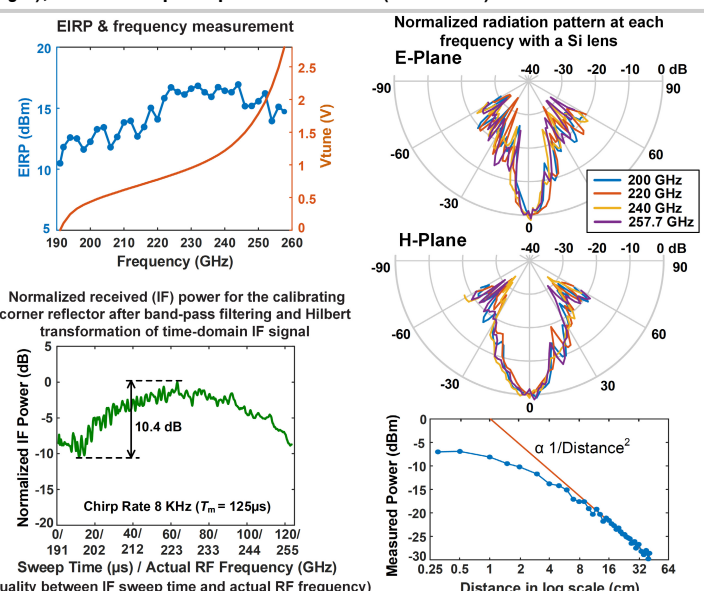


Figure 22.4.4: Measurement results of the chip.

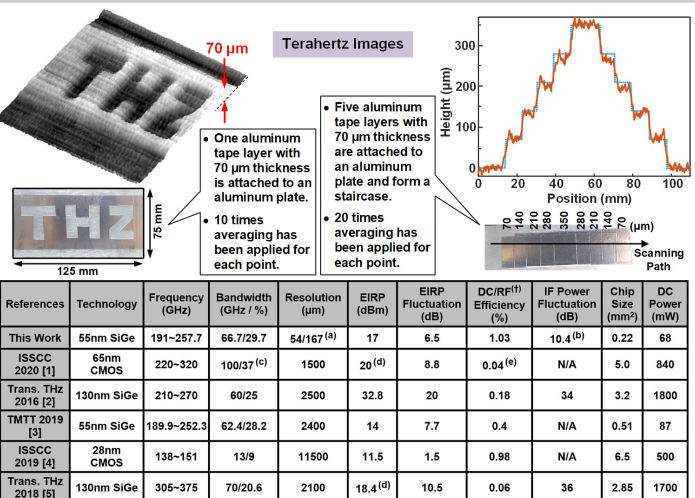


Figure 22.4.6: Terahertz images and comparison with other state-of-the-art FMCW radars.



Figure 22.4.5: Measured range resolution of radar with ±2σ error bars (95.5% confidence) with and without averaging. Photo of the range resolution test setup is also shown.

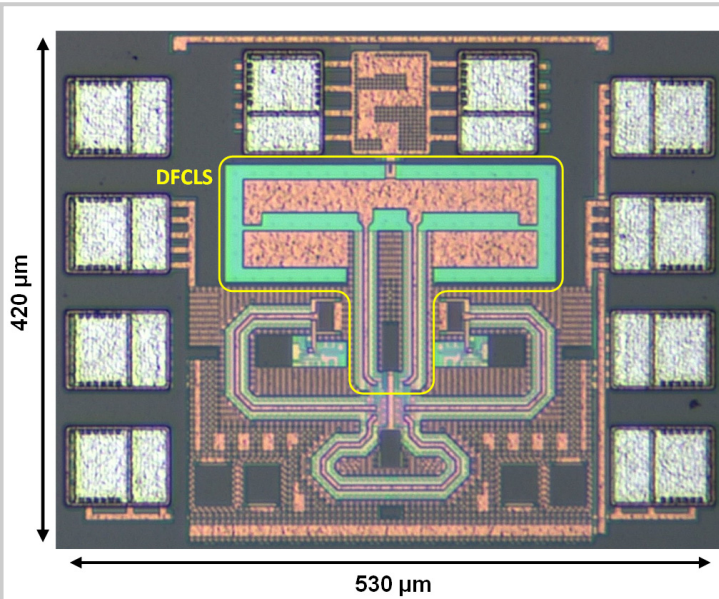


Figure 22.4.7: Die micrograph.